

Engineering Modular Peptide Nanoparticles for Ferroptosis-Enhanced Tumor Immunotherapy

Bihan Wu, Xuejiao Yang, Nan Kong, Juan Liang, Sangshuang Li, and Huaimin Wang*

Abstract: Indoleamine 2,3-dioxygenase 1 (IDO1) inhibitors are promising for treating tumors but have limited efficacy due to the immunosuppressive tumor microenvironment. In this study, we develop an orchestrated nanoparticle system using modular peptide assemblies, where the co-assembled sequences are designed for the specific binding to the hydrophobic and hydrophilic domains, guiding the assembly process and enabling the customization of nanoparticle properties. We exploit the modularity of this platform to integrate a hydrophobic ferroptosis precursor, an IDO1 inhibitor, and a hydrophilic peptidic PD-L1 antagonist for optimizing therapeutic outcomes through ferroptosis-enhanced tumor immunotherapy. The resulting nanoparticles induce immunogenic ferroptosis, enhance the intratumoral function of T lymphocytes, suppress regulatory T cells, and effectively modulate the immunosuppressive tumor microenvironment, thereby facilitating regression of tumor growth. This work provides a modular peptide-based nanoparticle engineering strategy and holds significant potential for advancing cancer treatment.

Introduction

Cancer immunotherapy has revolutionized patient outcomes and significantly enhanced quality of life. However, the presence of immunosuppressive cells within the tumor microenvironment (TME), particularly regulatory T (Treg) cells, poses a substantial barrier to the efficacy of therapies such as checkpoint inhibitors.^[1] High frequencies of Treg cells have been associated with poor prognoses in various solid tumors, as they inhibit the activity of effector T cells and antigen-presenting cells.^[2] Indoleamine 2,3-dioxygenase 1 (IDO1) plays a critical role in promoting Treg cell activation within the TME. Its overexpression in tumor and antigen-presenting cells recruits Treg cells, suppresses T cell

responses, and facilitates immune evasion by depleting L-tryptophan (Trp) and accumulating kynurenine (Kyn).^[1c] Inhibitors of IDO1, such as NLG8189, NLG919, and NLG919 analogue (NLG),^[3] show potential in mitigating Treg cell suppression and enhancing effector T cell activation. However, these inhibitors face significant challenges, including poor water solubility, the need for high-dose oral administration, off-target effects, and disappointing efficacy as monotherapy in clinical trials.^[4] While various nanocarriers have been explored for the co-delivery of chemotherapeutics and immune checkpoint inhibitors to achieve therapeutic synergy,^[5] the development of orchestrated nanoparticles employing sequential self-assembly of small molecules to simultaneously alleviate the immunosuppressive TME and enhance antitumor T cell responses remains limited.

Studies have demonstrated that IDO inhibitors can enhance ferroptosis-induced cell death in tumor cells, suggesting a synergistic effect in promoting tumor cell death and stimulating the immune system for improved cancer therapy outcomes.^[6] Ferroptosis is a regulated form of cell death characterized by lethal lipid peroxidation.^[7] This process exhibits features of immunogenic cell death (ICD), involving the release of danger-associated molecular patterns (DAMPs), including calreticulin (CRT), high-mobility group box 1 (HMGB1), and adenosine triphosphate (ATP). These DAMPs can activate immune cells and initiate inflammatory responses. Therefore, the induction of ferroptosis has the potential to enhance the immunogenicity of tumor cells, reshape the immunosuppressive TME, and augment the response rate to immunotherapy.^[8]

In this work, we developed a modular orchestrated peptide nanoparticle integrating a ferroptosis precursor to sensitize tumor cells to IDO1 inhibition, addressing the limited effectiveness of IDO1-targeted therapy by cooperatively reshaping the immunosuppressive TME. The self-assembly property of these peptides allows for the customization of stable co-assembled nanoparticles with sequential properties. The nanoparticles increase intracellular reactive oxygen species (ROS) levels for the induction of immunogenic ferroptosis and further decrease Kyn production. These effects collectively contribute to modulating the immunosuppressive TME, enhancing antitumor T cell function, and achieving ferroptosis-enhanced immunotherapy in murine tumor models (Figure 1A). This work provides an efficient and generic strategy for generating multi-component co-assembled architectures, resulting in cooperative effects and improved treatment outcomes.

[*] Dr. B. Wu, Dr. X. Yang, N. Kong, Dr. J. Liang, S. Li, Dr. H. Wang
 Department of Chemistry
 School of Science, Westlake University
 Institution Institute of Natural Sciences, Westlake Institute for
 Advanced Study, No. 600 Dunyu Road, Hangzhou 310024, Zhejiang
 Province, China
 E-mail: wanghuaimin@westlake.edu.cn

Dr. H. Wang
 Westlake Laboratory of Life Sciences and Biomedicine
 18 Shilongshan Road, Hangzhou 310024, Zhejiang Province, China

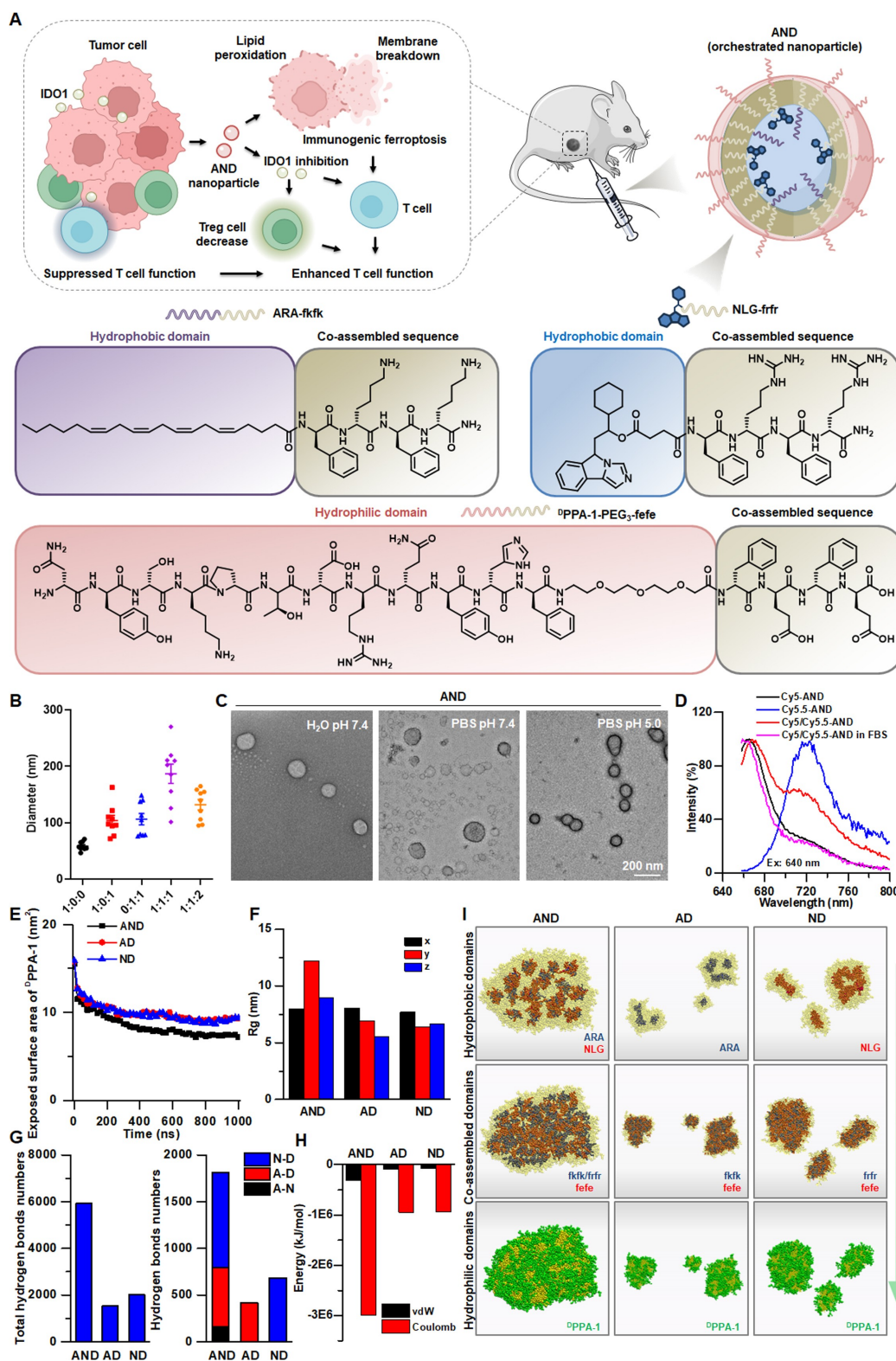


Figure 1. The proposed antitumor mechanism and characterization of nanoparticles. (A) The nanoparticles induce tumor cell ferroptosis and sequentially release NLG to target IDO1. These actions collectively revive antitumor T cell responses and sensitize tumor cells to IDO1 inhibition treatment. The nanoparticles are formed by combining three components. The hydrophobic domains contain ARA and NLG, and the hydrophilic domain consists of ^DPPA-1 with PEG₃ as a linker. The co-assembled domains are composed of oppositely charged tetrapeptides. (B) Diameter of the nanoparticles ($n=9$) at different molar ratios of peptides. (C) TEM images of AND nanoparticles. Scale bar, 200 nm. (D) Emission spectrum of AND nanoparticles incorporating fluorescence-labeled peptides. (E) Exposed surface area of ^DPPA-1 during the self-assembly process. (F) The values of R_g of aggregates formed by the different peptide mixtures. (G) The number of hydrogen bonds in the three systems. (H) The electrostatic and van der Waals interactions in the three systems. (I) Stacking patterns of hydrophobic domains, hydrophilic domains, and co-assembled parts in the nanoparticles.

Results and Discussion

Characterization of Orchestrated Nanoparticles

The rational design and controlled assembly of current multi-component peptide-based systems require careful consideration of peptide sequence and interactions between components to achieve the desired functionalities.^[9] Herein, we designed an orchestrated nanoparticle by modular peptide assemblies for generating ferroptosis-enhanced tumor immunotherapy. Arachidonic acid (ARA), as a precursor of ferroptosis, plays a crucial role in aiding the induction of immunogenic ferroptosis, primarily through lipid reprogramming.^[10] The hydrophobic ARA and NLG molecules are utilized to facilitate the self-assembly process and provide specific functionalities. The conjugation of NLG to the peptide via an ester bond enables selective release within cancer cells, taking advantage of the over-expression of esterase.^[11] To promote efficient co-assembly of the peptides, positively charged tetrapeptide containing D-phenylalanine (f) and D-lysine (k) or D-arginine (r) residues are used to bind the hydrophobic domains. Additionally, a negatively charged D-configuration tetrapeptide containing f and D-glutamic acid (e) residues is employed to bind the hydrophilic domains through a tris-polyethylene glycol (PEG₃) linker.^[12] The hydrophilic domain is composed of the ^DPPA-1 peptide, which blocks the interaction between programmed cell death-ligand (PD-L)1 and programmed cell death protein (PD)-1.^[13] The peptides are synthesized by standard Fmoc-based solid-phase peptide synthesis (SPPS) method (Scheme S1). The structure, purity, and molecular weight of the peptides are confirmed by liquid chromatography-mass spectrometry (LC-MS), proton nuclear magnetic resonance (¹H NMR), and matrix-assisted laser desorption ionization with time-of-flight mass spectrometry (MALDI-TOF, Figure S1–11, Table S1).

We initially evaluated the solubility and release profiles of the peptides to assess their potential for assembly and therapeutic applications. The ARA-fkfk peptide exhibits good solubility at neutral pH, whereas the ARA-frfr peptide forms a white precipitate in an aqueous solution. Cleavage studies of NLG-conjugated peptides upon esterase treatment using high performance liquid chromatography (HPLC) reveal sustained release patterns, with an 83.4% release for NLG-frfr peptide and just a 33.6% release for NLG-fkfk peptide after 72 h incubation (Figure S12). Based on these results, we selected the ARA-fkfk peptide and NLG-frfr peptide for further investigation.

To assess the self-assembly properties and morphology of the peptides, we performed dynamic light scattering (DLS) and transmission electron microscopy (TEM) at different molar ratios of peptides in an aqueous solution (Table S2). The critical micellization concentration (CMC) value of the ARA-fkfk peptide is approximately 98.96 μ M. DLS count rates of solutions containing NLG-frfr peptide and ^DPPA-1-PEG₃-fefe peptide are below 12 kcps, indicating the absence of noticeable assemblies in these samples (Figure S13). TEM images reveal that the ARA-fkfk peptide displays a spherical morphology with a diameter of 60 nm

due to its amphiphilic structure. No obvious structures are observed in the NLG-frfr peptide and ^DPPA-1-PEG₃-fefe peptide solutions. ARA-fkfk peptide and ^DPPA-1-PEG₃-fefe (1:1 molar ratio) can self-assemble to form nanoparticles with a size of approximately 104 nm. Upon combining the three cationic peptides in molar ratios of 1:1:1 and 1:1:2, the resultant mixtures assemble into nanoparticles with diameters of approximately 186 nm and 132 nm, respectively. Furthermore, the diameter of nanoparticles decreases with an increase in the hydrophilic peptide ratio (Figure 1B, Figure S14).

To investigate the co-assembly performance, we analyzed the morphological changes and conducted a fluorescence resonance energy transfer (FRET) experiment using a mixture of ARA-fkfk, NLG-frfr, and ^DPPA-1-PEG₃-fefe peptide at a molar ratio of 1:1:2 (defined as **AND**).^[14] The CMC value of **AND** nanoparticles is approximately 3.79 μ M (PBS buffer, pH 7.4, Figure S15). TEM results reveal that the ARA-fkfk peptide forms nanoaggregates in the PBS buffer instead of ordered nanoparticles (Figure S16). However, **AND** nanoparticles retain their spherical morphology in salt-containing environments (Figure 1C), suggesting that the introduction of co-assembled sequences between the hydrophobic and hydrophilic domains of the peptides promotes the formation of stable interactions, thereby enhancing the overall stability of the assemblies. We observed a higher number of nanoparticles in the PBS buffer compared to water (Figure 1C, Figure S17), possibly due to the influence of salt in the PBS buffer on the self-assembly process of peptides. The presence of salt can screen the surface charge of the peptides and reduce the solubility of hydrophobic regions, thereby promoting their self-assembly into well-defined structures.^[15] To further evaluate the co-assembly performance, the Cy5 and Cy5.5, a pair of FRET fluorescence probes with a Förster distance of 7.3 nm,^[16] are used to label the peptides, respectively (Scheme S2, Figure S18–20). The spectra of Cy5/Cy5.5-**AND** nanoparticles indicate the presence of FRET interactions with a FRET ratio of 0.38. However, the FRET ratio decreases in the presence of fetal bovine serum (FBS), indicating the loss of co-assembled structure (Figure 1D). We examined the effects of the co-assembled sequence and domain substitution on the formation of assemblies (Figure S21–25). We prepared the mixture of peptides composed of ^DPPA-1 peptide without a co-assembled sequence, ^DPPA-1-conjugated peptide without a PEG₃ linker (^DPPA-1-fefe), and ^DPPA-1-conjugated peptide with two PEG₃ linkers (^DPPA-1-(PEG₃)₂-fefe), respectively. TEM images show that the ^DPPA-1-fefe peptide forms nanoaggregates in an aqueous solution, and the resultant peptide mixture forms aggregates rather than nanoparticles. The peptide mixture composed of ^DPPA-1 and ^DPPA-1-(PEG₃)₂-fefe peptide forms nanoaggregates and nanoparticles, respectively. Additionally, we utilized sulfasalazine (SAL), a ferroptotic cell death inducer,^[17] as a substitution for the hydrophobic residue. TEM images of the mixture of peptides reveal the presence of nanoparticles (Figure S26). These results suggest the versatility of the design strategy

and underscore the importance of the co-assembled sequence in achieving the desired nanostructures (Table S3).

The mixture of ARA-fkfk and ^DPPA-1-PEG₃-fefe peptide at a molar ratio of 1:1 (defined as **AD**), the mixture of NLG-frfr and ^DPPA-1-PEG₃-fefe peptide at a molar ratio of 1:1 (defined as **ND**), and **AND** nanoparticles exhibit a spherical morphology. Molecular dynamics (MD) simulations are conducted to explore the differences in the self-assembly processes of three systems (Figure S27). The peptides in the **AND** system start to co-assemble into nanoaggregates and eventually form large spherical nanostructures (Figure S28). The evolution of the exposed surface area of ^DPPA-1 in the **AND** system exhibits a rapid decrease and the lowest value among three systems, suggesting its relatively rapid assembly and high aggregation capacity (Figure 1E). The **AND** system exhibits assemblies with a larger diameter, as evidenced by higher radius of gyration (*R_g*) values compared to the other systems (Figure 1F), which is consistent with the results obtained from TEM. Interaction analysis shows that the total number of hydrogen bonds in the **AND** system is higher than that in the other systems (Figure 1G). Importantly, **AND** system exhibits a higher number of hydrogen bonds between NLG-frfr peptide and ^DPPA-1-PEG₃-fefe peptide compared to the two-components systems. A similar trend is observed for the number of hydrogen bonds between ARA-fkfk peptide and ^DPPA-1-PEG₃-fefe peptide. These strengthened interactions, including electrostatic and van der Waals forces, contribute favorably to their binding, facilitating a more stable assembly compared to the two-components systems (Figure 1H). The stacking patterns show that all peptide mixtures display relatively compact internal distributions composed of hydrophobic domains. As expected, the NLG and ARA residues are found to be buried within the aggregates, promoting aggregation, while the hydrophilic domain is exposed on the surface, contributing to the solvation of the assemblies. Furthermore, direct interactions among co-assembled parts are observed, along with the spatial distributions at the interfaces between hydrophilic and hydrophobic domains (Figure 1I, Figure S29).^[18]

Action Mechanism of **AND** Nanoparticles

The cytotoxicity of peptides is examined on ferroptosis-sensitive 4T1 triple-negative breast cancer cell line.^[19] The ^DPPA-1-PEG₃-fefe peptide has no obvious influence on cell viability. We observed that the ARA-fkfk peptide forms aggregates in the culture medium, leading to the inhibition of cell proliferation (Figure S30). The **AND** nanoparticles exhibit dose-dependent inhibition and enhanced toxicity compared to the **AD** and **ND** group alone (Figure 2A, Table S4).

We investigated the cellular uptake and dissociation process of **AND** nanoparticles within the cells. The addition of chlorpromazine (CPZ), an inhibitor of clathrin-mediated endocytosis,^[20] reduces peptide uptake by 11.1 %, indicating that the **AND** nanoparticles mainly undergo clathrin-mediated endocytosis (Figure 2B). The spectra and subcellular

distribution of Cy5/Cy5.5-**AND** nanoparticles inside the cells are visualized by confocal laser scanning microscopy (CLSM) FRET spectrograms. After 2 h of incubation, the nanoparticles are internalized into cells with a FRET ratio of 0.33 ± 0.04 . As time progressed, the peptides diffuse inside the cells, leading to a decrease in the FRET ratio to 0.24 ± 0.02 after 12 h of incubation. This decrease indicates the gradual dissociation of **AND** nanoparticles within the cells (Figure 2C, Figure S31).

To investigate the cell death pathways induced by peptides, the production of intracellular ROS and lipid peroxidation are evaluated. Flow cytometry analysis reveal a significant increase in the fluorescence intensity of intracellular DCF (3.29-fold increase) and DHE (1.33-fold increase) compared to the control group, suggesting that **AND** nanoparticles can induce the production of intracellular ROS (Figure 2D, Figure S32). Cells respond efficiently to treatment with **AND** nanoparticles, resulting in a 2.94-fold increase in lipid ROS (Figure 2E). Considering the integration of ARA into phospholipids to induce tumor cell ferroptosis, we hypothesized that the ARA-fkfk peptide in **AND** nanoparticles might serve as a substrate to exert cytotoxic effects on the plasma membrane by increasing lipid peroxidation.^[21] To investigate the role of lipid peroxidation in cell death, we stained cells with C11-BODIPY and cell membrane stains and imaged them at different timepoints. The ratio of oxidized C11 BODIPY within the plasma membrane is quantified. Treatment with **AND** nanoparticles induces peroxidation of the plasma membrane within 2 h, and after 8 h of incubation, the cells exhibit a 3.45-fold higher level of peroxidation (Figure 2F, Figure S33). To further investigate the cytotoxicity of **AND** nanoparticles on the cell membrane, we conducted a fluorescence recovery after photobleaching (FRAP) experiment (Figure 2G). The results reveal that the control group exhibits rapid fluorescence recovery with a mobile fraction of 62.9 ± 11.9 %, whereas treatment with **AND** nanoparticles results in poor FRAP recovery with a mobile fraction of 20.6 ± 13.5 % (Figure 2H). These findings indicate that the cells experience cell membrane damage after treatment with **AND** nanoparticles. To examine whether the cytotoxic effect on the plasma membrane influences cancer cell mechanical properties, we measured single-cell cortical stiffness using atomic force microscopy (AFM). Compared to the stiffness of normal 4T1 cell, the **AND** nanoparticles-treated cells exhibit a 1.66-fold higher stiffness (Figure 2I), which could contribute to the enhancement of T-cell cytotoxicity and their ability to eliminate cancer cells.^[22] In addition, the cytotoxicity induced by **AND** nanoparticles is partially rescued by ferroptosis inhibitors, including ferrostatin-1 (Fer-1) and liproxstatin-1 (Lip-1), reducing cell death from 39.1 % to 22.8 % and 23.8 %, respectively (Figure S34). These results indicate that **AND** nanoparticles induce tumor cell death via ferroptosis, as lipid peroxidation and plasma membrane breakdown are functional markers for ferroptosis.^[23]

Bio-EM is employed to observe cell ultrastructural changes caused by the **AND** nanoparticles (Figure 2J). We observed the distribution of peptides at the cell membrane

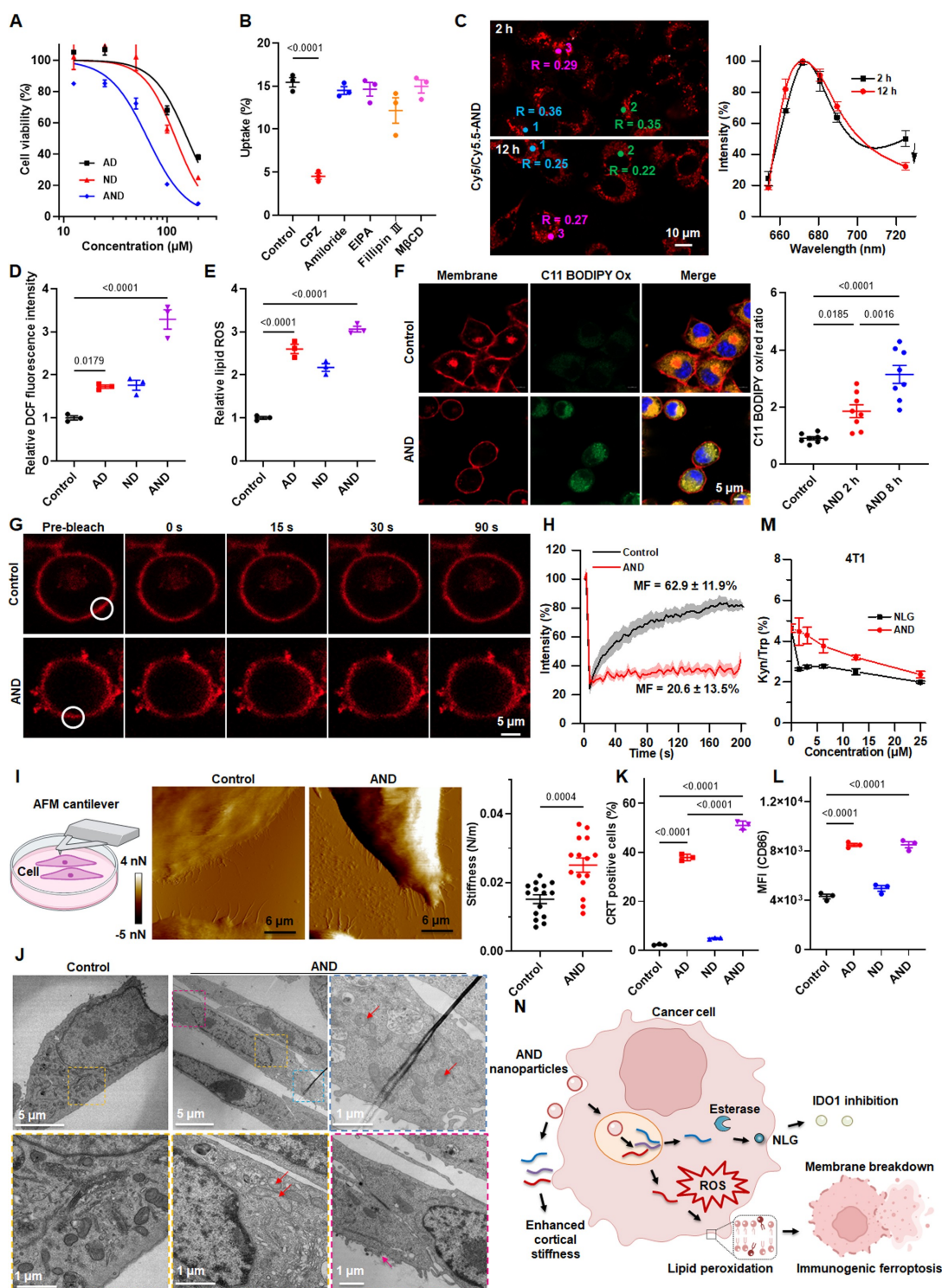


Figure 2. Characterization of AND nanoparticles *in vitro*. (A) Cytotoxicity of the mixture of peptides. (B) Effects of endocytic inhibitors on cellular uptake after 2 h of incubation quantified using HPLC. (C) CLSM images and emission spectrum of Cy5/Cy5.5-AND nanoparticles after 2 h and 12 h of incubation. Scale bar, 10 μm . (D, E) Relative fluorescence level of intracellular DCF (D) and oxidized C11 BODIPY (E) measured by flow cytometry under peptide treatment for 12 h. (F) CLSM images of 4T1 cells treated with AND nanoparticles and quantification of C11 BODIPY oxidized: reduced ratio within the membrane. Scale bar, 5 μm . CellMask Deep Red is used to select regions of interest and the C11 BODIPY signal is quantified using ImageJ. Each point represents a single cell. (G) CLSM images of 4T1 cells before and after photobleaching. A small region of interest is bleached (white circle), and the fluorescence recovery curve is monitored. Scale bar, 5 μm . (H) Fluorescence intensity is plotted over time. (I) Cortical stiffness of cells measured by AFM. (J) Bio-TEM images of normal 4T1 cells and cells treated with AND nanoparticles for 12 h. Scale bars of whole cells and enlarged images are 5 μm and 1 μm , respectively. (K) Exposure of CRT on 4T1 cells. (L) Expression of CD86 on BMDCs. (M) Inhibition of IDO1 on 4T1 cells after 48 h incubation. (N) Proposed mechanism of action for AND nanoparticles. Data are depicted as mean \pm SEM.

(pink arrow). Compared to the normal mitochondria in the control group, we observed a lack of mitochondrial integrity and shrunken mitochondria with loss of mitochondrial cristae (red arrows) after treatment of **AND** nanoparticles, which are characteristic features of ferroptosis. Furthermore, treatment with **AND** nanoparticles induces the exposure of CRT on the cell surface (Figure 2K), the release of ATP (Figure S35), and the decrease of HMGB1 within the nucleus (Figure S36–37), indicating cellular stress and potential immunogenicity. Additionally, co-incubation of **AND** nanoparticles-treated tumor cells with bone marrow-derived dendritic cells (BMDCs) stimulates the expression of CD86 and CD40 on BMDCs (Figure S38–39, Figure 2L), indicating the activation of the immune response. The **AND** nanoparticles also possess the ability to inhibit IDO1 activity, as evidenced by the dose-dependent inhibition of Kyn production (Figure 2M).

Collectively, the higher levels of ROS production and lipid peroxidation induced by **AND** nanoparticles result in increased oxidative stress, leading to immunogenic ferroptosis. Furthermore, the ability of **AND** nanoparticles to inhibit IDO1 provides an additional advantage in overcoming the immunosuppressive effects of the TME (Figure 2N). In addition, the ^DPPA-1-conjugated peptides have been shown to block the PD–L1 with high affinity and enhance the secretion of interferon- γ (IFN γ).^[13,24] Thus, the combination of the **AND** nanoparticles' potent induction of ferroptosis, their capacity for IDO1 inhibition, and their potential to modulate the TME make them a promising candidate for enhanced antitumor immunotherapy.

AND Nanoparticles Suppress Tumor Growth by Switching the Immunosuppression Status

The therapeutic effect of **AND** nanoparticles is evaluated in a mouse model bearing 4T1 tumor (Figure 3A), which represents a poorly immunogenic tumor model with an immune-excluded phenotype characterized by Treg cell-mediated suppression and limited infiltration of immune cells.^[25] Throughout the experimental period, the mice exhibit no observable signs of toxicity (Figure S40). The HPLC results demonstrate a gradual degradation and clearance of peptides, along with the release of NLG within the tumors (Figure S41). Specifically, the NLG-frfr peptide exhibits a half-life ($t_{1/2}$) of approximately 9.5 h, while the ARA-fkfk peptide has a $t_{1/2}$ of about 15.7 h. Compared to the PBS group, treatment with **AND** nanoparticles significantly attenuates the tumor growth rate (Figure 3B, Figure S42) and results in a tumor inhibition rate of 38.7% (Figure 3C). However, the **AND** nanoparticles treatment does not demonstrate a significant tumor suppression effect compared to the **AD** and **ND** group in mice bearing subcutaneous 4T1 tumor. This may be attributed to the anti-ferroptotic mechanisms within tumor cells and the complexity of the TME, which could pose additional challenges to the treatment's efficacy.^[26] The immune mechanism underlying these effects is investigated using flow cytometry (Figure S43–45). The **AND** treatment induces a 2.25-fold

increase in the percentage of CD80⁺CD86⁺ dendritic cell (DCs) compared to the PBS group (Figure 3D). Furthermore, activation markers CD69 are significantly overexpressed on CD4⁺ T cells (1.64-fold increase, Figure 3E) and CD8⁺ T cells (1.75-fold increase, Figure 3F), indicating trafficking of DCs and activation of T cells within the lymph nodes. Additionally, treatment with **AND** nanoparticles results in an enhanced frequency of CD3⁺CD8⁺ T cells (1.64-fold increase, Figure 3G), CD8⁺TNF α ⁺ T cells (1.32-fold increase, Figure 3H), CD4⁺TNF α ⁺ T cells (1.68-fold increase, Figure S46), and CD8⁺GrB⁺ T cells (1.33-fold increase, Figure 3I) within the tumors than the PBS group. These results suggest that **AND** treatment promotes the maturation of DCs, activates T cells, and enhances anti-tumor immune responses. Immunofluorescence (IF) staining images (Figure 3J) demonstrate a significant decrease in the population of Treg cells (a 67.7% decrease, Figure 3K), and a higher infiltration of CD4⁺ T cells (5.53-fold increase, Figure S47) and CD8⁺ T cells (4.38-fold increase, Figure 3L) in the **AND** nanoparticles group compared to the PBS group. These changes suggest the immunomodulating effects of the treatment, indicating a shift towards a more favorable antitumor immune response within the TME.

The low levels of PD–L1 expression on 4T1 tumors have been reported to limit the efficacy of PD–L1 blockade treatment.^[27] Thus, the therapeutic potential of **AND** nanoparticles is further evaluated using MC38 tumor model (Figure 4A, Figure S48), which is highly immunogenic and manifests high sensitivity to ferroptosis inducer and PD–L1 blockade therapy.^[28] Treatment with **AND** nanoparticles results in additional tumor inhibition (Figure 4B, Figure S49), achieving a tumor inhibition rate of 66.4% compared to PBS group (Figure 4C). The mice treated with **AND** nanoparticles also show increased frequency of IFN γ -secreting CD8⁺ T cells, TNF α -secreting CD8⁺ T cells, and TNF α -secreting CD4⁺ T cells, which are 1.23-, 1.29- and 1.46-fold higher than those in PBS-treated mice, respectively, suggesting the enhancement of cytotoxic T cell activity (Figure 4D, Figure S50). Analysis of intratumoral chemokines reveals that treatment with **AND** nanoparticles leads to significant changes in chemokine expression within the TME, which in turn affects immune responses. Specifically, the chemokine CCL22, known for recruiting Tregs to the tumor tissue, exhibits a 54.1% decrease after treatment with **AND** nanoparticles, indicating a reduction in CCL22-induced immune suppression.^[29] Furthermore, administration of **AND** nanoparticles results in lower production of immunosuppressive chemokines, such as CCL2 (a 51.7% decrease), CCL3 (a 48.9% decrease), and CCL5 (a 58.1% decrease), compared to the PBS group. These chemokines are associated with the increased presence of immunosuppressive cells within tumors, promoting tumor invasion and metastasis, as well as poor patient prognosis (Figure 4E).^[30] **AND** nanoparticle treatment results in a 56.0% decrease in the Kyn/Trp ratio (Figure 4F) and a 1.73-fold increase in the malondialdehyde level (Figure S51), indicating a reduction in IDO1 activity and enhanced lipid peroxidation within tumor tissues. Additionally, a 66.3% decrease in Treg cells after treatment with **AND** nanoparticles further contributes

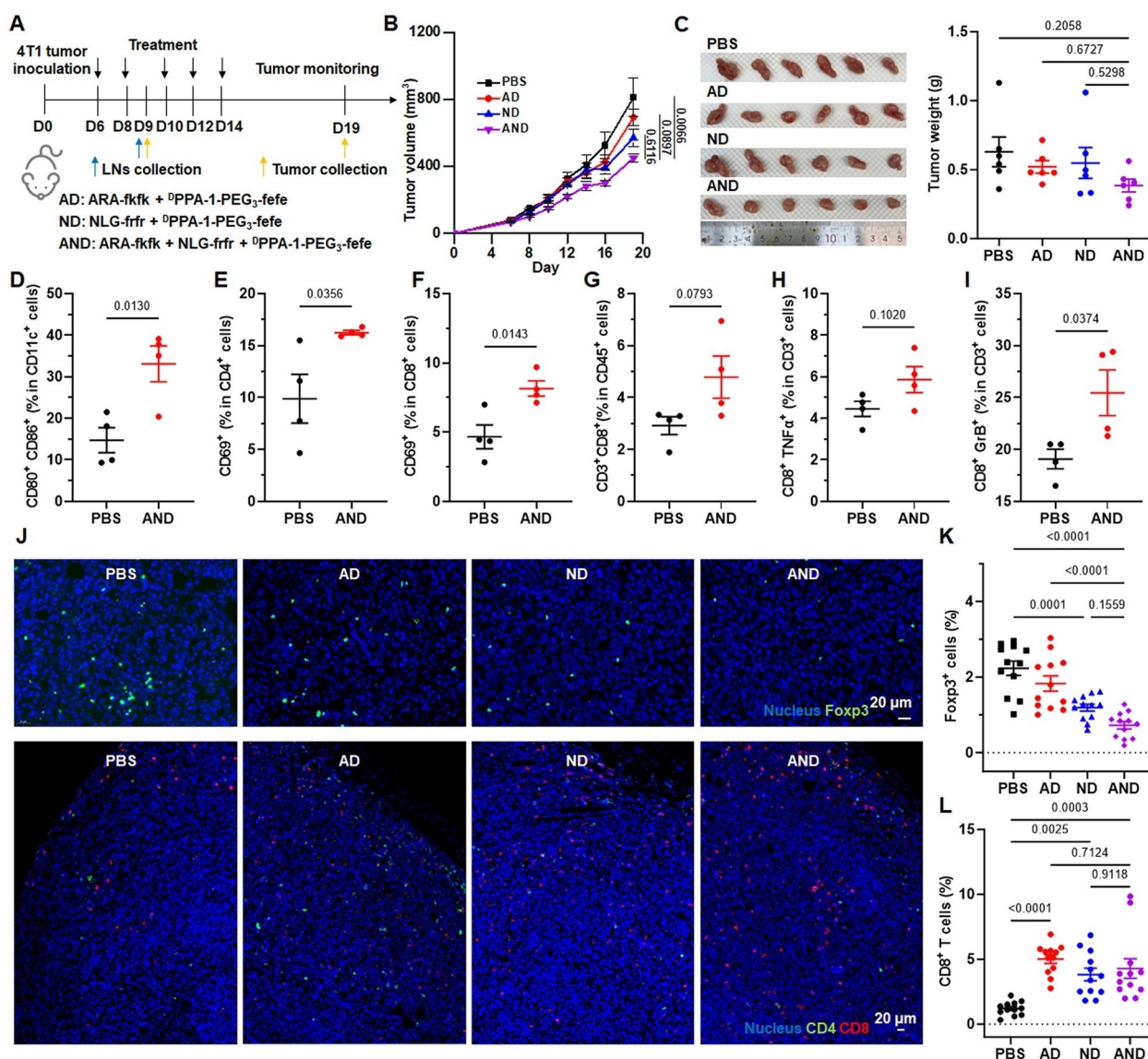


Figure 3. Antitumor efficacy of peptides in mice bearing subcutaneous 4T1 tumor. (A) Scheme of tumor cell inoculation, treatment, immune response analysis, and antitumor effect evaluation. Dosing schedules are indicated by black arrows. (B) Changes in tumor volume of mice over time ($n=6$). (C) Tumor weight and optical images of dissected tumors at the end of the treatment. (D) The proportion of $CD80^+CD86^+$ DCs in lymph nodes on day 9. (E, F) The proportion of activated $CD4^+$ T cells ($CD69^+$, E) and activated $CD8^+$ T cells ($CD69^+$, F) in lymph nodes on day 9. (G–I) The proportion of $CD3^+CD8^+$ T cells (G), $CD8^+TNF\alpha^+$ T cells (H), and $CD8^+GrB^+$ T cells (I) in tumors on day 9. (J) IF images of $Foxp3^+$ cells, $CD4^+$ T cells, and $CD8^+$ T cells in tumor tissues on day 19. Scale bar, 20 μm . (K, L) Quantitative analysis of $Foxp3^+$ cells (K) and $CD8^+$ T cells (L) using ImageJ. Data are depicted as mean \pm SEM.

to the alleviation of immunosuppression and enhanced tumor inhibition (Figure 4G).

To explore the cellular and molecular landscape of the TME, we performed single-cell RNA-sequencing. Through the analysis of expression of cellular marker genes, we identified five cell types, including fibroblasts, endothelial cells, immature B cells, macrophages, and T_{NK} cells (Figure 5A). Subclustering of T_{NK} cells reveals five distinct populations, including $CD8^+$ proliferating T cells, $CD8^+$ exhausted cells, naive T cells, NK cells, and Treg cells (Figure 5B). Treatment with **AND** nanoparticles results in a decrease in the number of fibroblast (14.3 %, Figure 5C) and

Treg cell subpopulations (42.3 %, Figure 5D) compared to the PBS group, which is consistent with the IF staining images. We identified the fibroblast cluster exhibiting dramatically higher level of large-scale copy-number variations (CNVs), which is indicative of genomic instability and a hallmark of cancer cell, indicating their malignant transformation (Figure 5E).^[31] We analyzed the differential gene expression in malignant fibroblast cells and T_{NK} cells following **AND** nanoparticles treatment (Figure S52). Kyoto Encyclopedia of Genes and Genomes (KEGG) analysis reveals that the differential genes in malignant fibroblast cells are primarily enriched in TNF signaling pathway, IL-17

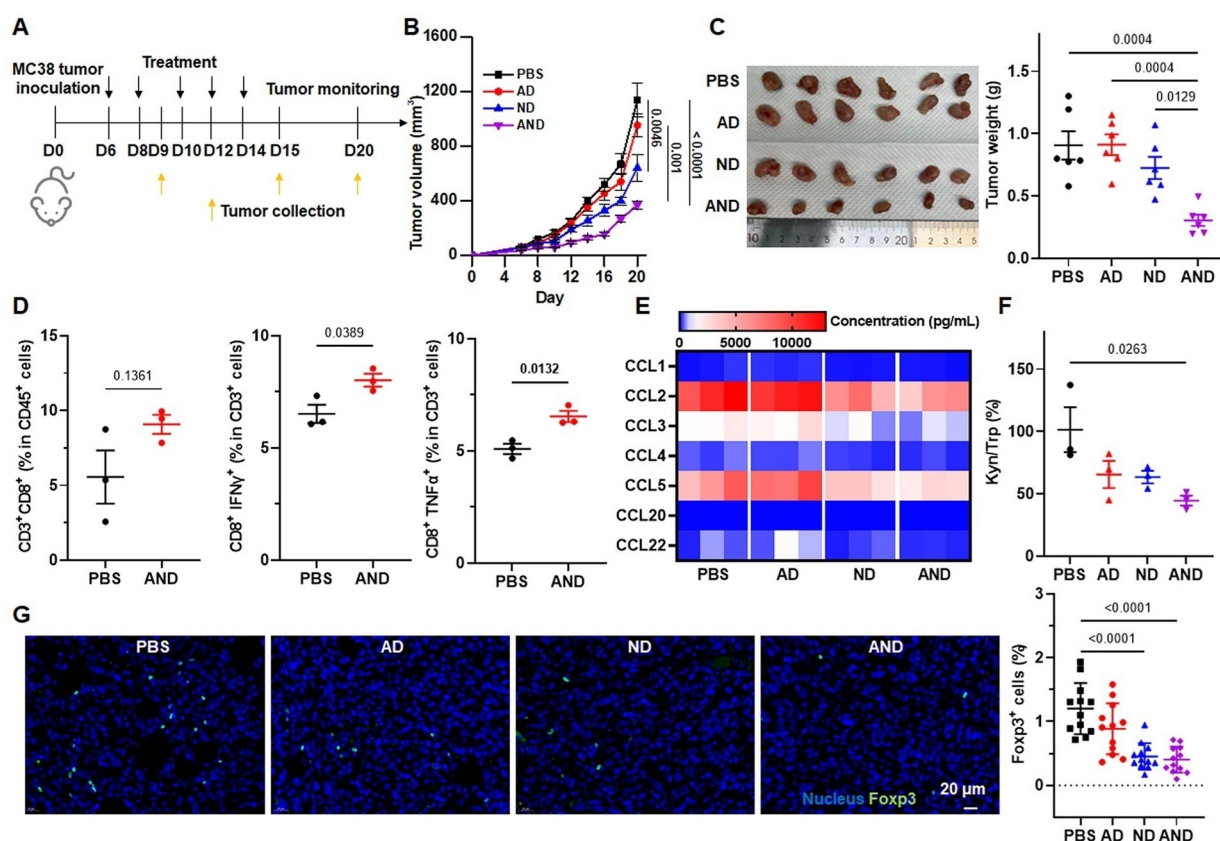


Figure 4. Antitumor efficacy of peptides in mice bearing subcutaneous MC38 tumor. (A) Scheme of tumor cell inoculation, treatment, immune response analysis, and antitumor effect evaluation. (B) Tumor volume of mice ($n=6$) over time. (C) Optical images of dissected tumors and corresponding tumor weight at the end of the treatment. (D) The frequencies of CD8⁺, CD8⁺IFN γ ⁺ T cells, and CD8⁺TNF α ⁺ T cells in the tumors on day 9. (E) Intratumoral chemokine levels on day 15. (F) Kyn/Trp ratio in tumors on day 20. (G) IF images and quantitative analysis of Foxp3⁺ cells in tumor tissues. Scale bar, 20 μ m. Data are depicted as mean \pm SEM.

signaling pathway, Toll-like receptor signaling pathway, and NOD-like receptor signaling pathway (Figure 5F). The differential genes in T_{NK} cells are primarily enriched in TNF signaling pathway, Toll-like receptor signaling pathway, and NF-kappa B signaling pathway, suggesting the potential activation of immune response within the tumor tissue (Figure 5G). To investigate the interactions between malignant fibroblast cells and T_{NK} cells, a CellChat analysis is performed. The circle plot visualizes the interaction strength in the cell-cell communication network, where red and blue lines represent the increased and decreased signaling after **AND** nanoparticles treatment compared to the PBS group, respectively. The interaction strength between malignant fibroblast cells and T_{NK} cells decreases after treatment with **AND** nanoparticles (Figure 5H), indicating a potential disruption of inhibitory signals and a shift in the immune response.

Conclusion

This work describes a modular nanoparticle system that allows for the tailoring of peptide functionalities. The core of the nanoparticle is driven by hydrophobic segments, faci-

tating aggregation, while the hydrophilic components form a shell, ensuring the peptide system's stability and enabling surface modification for targeted delivery. The use of co-assembled sequences to specifically bind to the hydrophobic and hydrophilic domains guides the assembly process. Here, we exploited the modularity and flexibility of this platform to design an orchestrated nanoparticle carrying a hydrophobic ferroptosis precursor, an IDO1 inhibitor, and a hydrophilic peptidic PD-L1 antagonist for the synergistic potential of overcoming tumor immune evasion. This combination induces immunogenic ferroptosis and reshapes the TME from immunosuppressive to immunostimulatory, providing a solution to the limited effectiveness of current IDO1 inhibitors. Overall, this modular approach holds promise for optimizing both assembly properties and therapeutic functionalities.

Acknowledgements

This project was supported by the National Natural Science Foundation of China (82272145) and the Foundation of Westlake University. We thank the Instrumentation and Service Center for Molecular Sciences, Instrumentation and

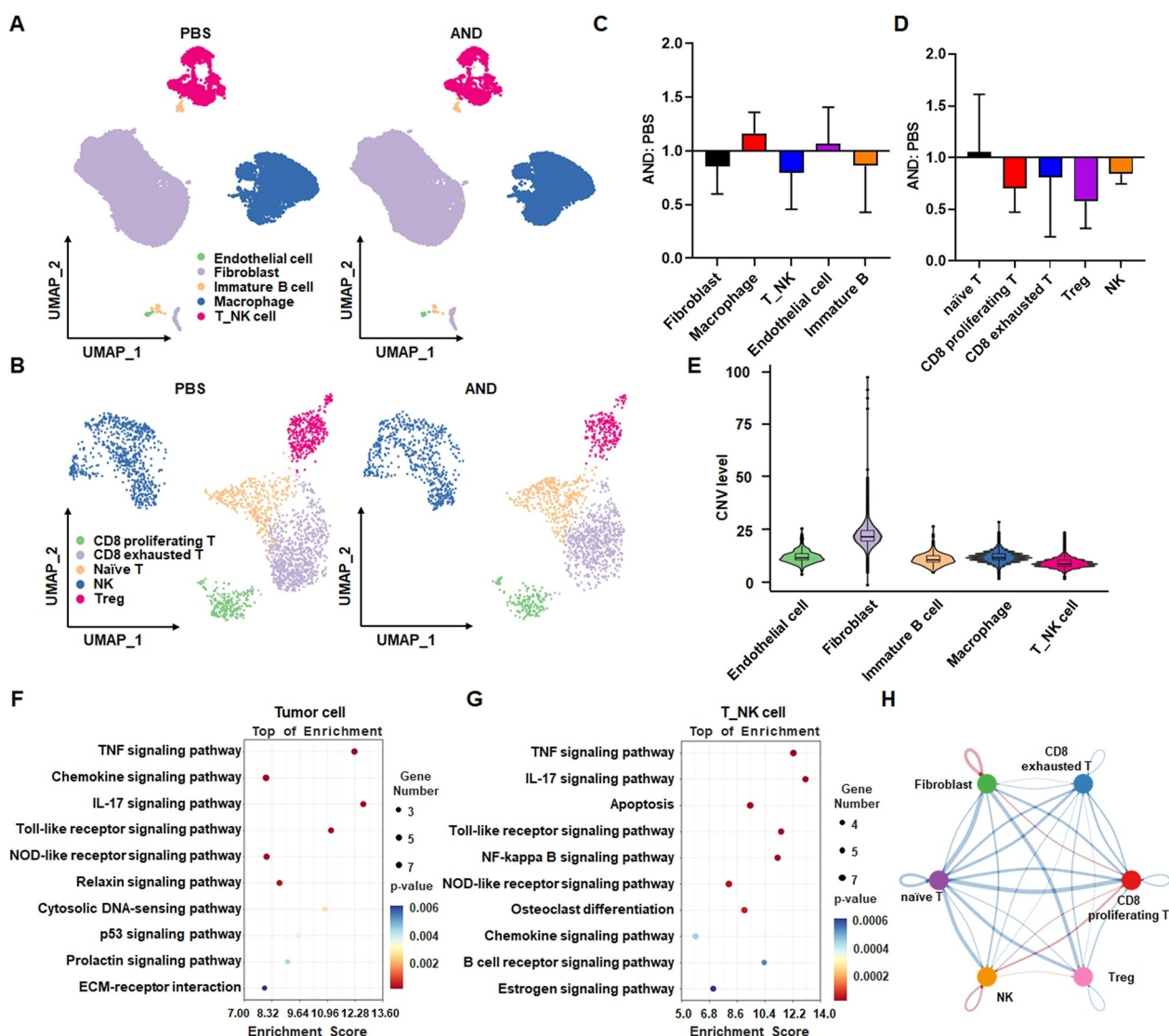


Figure 5. Single-cell RNA-sequencing analysis. (A) Uniform manifold approximation and projection (UMAP) plot displaying major cell types. (B) UMAP plot of the main cell types in T_NK cells. Dots represent individual cells, and colors represent different cell populations. (C) Relative proportions of each cluster. (D) Relative proportions of each cluster in T_NK clusters. (E) Violin plots of CNV levels among five cell types. (F) KEGG analysis of differential genes in malignant fibroblast cells. (G) KEGG analysis of differential genes in T_NK cells. (H) CellChat analysis between malignant fibroblast cells and T_NK subcluster cells.

Service Center for Physical Sciences, General Equipment Core Facility, Biomedical Research Core Facilities, and Laboratory Animal Resource Center at Westlake University for the assistance with measurements. We thank the State Key Laboratory of Chemical Engineering of Zhejiang University.

Conflict of Interest

The authors declare no conflict of interest.

Data Availability Statement

The data that support the findings of this study are available from the corresponding author upon reasonable request.

Keywords: self-assembly · nanoparticle · ferroptosis · immunotherapy

- [1] a) C. Robert, *Nat. Commun.* **2020**, *11*, 3801; b) A. D. Waldman, J. M. Fritz, M. J. Lenardo, *Nat. Rev. Immunol.* **2020**, *20*, 651–668; c) F. Shan, A. Somasundaram, T. C. Bruno, C. J. Workman, D. A. A. Vignali, *Trends Cancer* **2022**, *8*, 944–961.
[2] A. Tanaka, S. Sakaguchi, *Cell Res.* **2017**, *27*, 109–118.

- [3] a) A. Meireson, M. Devos, L. Brochez, *Front. Immunol.* **2020**, *11*, 531491; b) J. E. Cheong, L. Sun, *Trends Pharmacol. Sci.* **2018**, *39*, 307–325.
- [4] a) A. Nayak, Z. Hao, R. Sadek, N. Vahanian, W. J. Ramsey, E. Kennedy, M. Mautino, C. Link, P. Bourbo, R. Dobbins, K. Adams, A. Diamond, L. Marshall, D. H. Munn, J. Janik, S. N. Khleif, *J. Immunother. Cancer* **2014**, *2*, P250; b) K. Tang, Y. H. Wu, Y. Song, B. Yu, *J. Hematol. Oncol.* **2021**, *14*, 68.
- [5] a) Z. Wang, W. Li, Y. Jiang, T. B. Tran, L. E. Cordova, J. Chung, M. Kim, G. Wondrak, J. Erdrich, J. Lu, *Nat. Commun.* **2023**, *14*, 7235; b) Y. Chen, R. Xia, Y. Huang, W. Zhao, J. Li, X. Zhang, P. Wang, R. Venkataramanan, J. Fan, W. Xie, X. Ma, B. Lu, S. Li, *Nat. Commun.* **2016**, *7*, 13443; c) L. Dai, M. Yao, Z. Fu, X. Li, X. Zheng, S. Meng, Z. Yuan, K. Cai, H. Yang, Y. Zhao, *Nat. Commun.* **2022**, *13*, 2688; d) J. Ding, T. Wang, Z. Chen, Z. Lin, X. Chen, C. He, *J. Polym. Sci.* **2022**, *60*, 1595–1609; e) D. Wang, T. T. Wang, H. J. Yu, B. Feng, L. Zhou, F. Y. Zhou, B. Hou, H. W. Zhang, M. Luo, Y. P. Li, *Sci. Immunol.* **2019**, *4*, eaau6584.
- [6] a) A. Fiore, L. Zeitler, M. Russier, A. Gross, M. K. Hiller, J. L. Parker, L. Stier, T. Kocher, S. Newstead, P. J. Murray, *Mol. Cell* **2022**, *82*, 920–932; b) P. Huang, Y. Yang, W. Wang, Z. Li, N. Gao, H. Chen, X. Zeng, *Biomaterials* **2023**, *299*, 122157.
- [7] a) B. R. Stockwell, J. P. Friedmann Angeli, H. Bayir, A. I. Bush, M. Conrad, S. J. Dixon, S. Fulda, S. Gascon, S. K. Hatzios, V. E. Kagan, K. Noel, X. Jiang, A. Linkermann, M. E. Murphy, M. Overholtzer, A. Oyagi, G. C. Pagnussat, J. Park, Q. Ran, C. S. Rosenfeld, K. Salnikow, D. Tang, F. M. Torti, S. V. Torti, S. Toyokuni, K. A. Woerpel, D. D. Zhang, *Cell* **2017**, *171*, 273–285; b) H. N. Bell, B. R. Stockwell, W. Zou, *Immunity* **2024**, *57*, 941–956.
- [8] a) E. Iuliia, C. Elena, M. Louis Van der, D. T. Victoria, H. Hamida, A. M. Tatiana, V. V. Maria, F. Carmela, B. Claus, C. Frauke, L. Steve, G. S. Andre, K. Olga, V. K. Dmitri, *J. Immunother. Cancer* **2020**, *8*, e001369; b) X. Zhai, Y. Lin, L. Zhu, Y. Wang, J. Zhang, J. Liu, L. Li, X. Lu, *Cytokine Growth Factor Rev.* **2024**, *75*, 101–109; c) W.-J. Wang, Y.-Y. Ling, Y.-M. Zhong, Z.-Y. Li, C.-P. Tan, Z.-W. Mao, *Angew. Chem. Int. Ed.* **2022**, *61*, e202115247.
- [9] a) E. R. Draper, E. G. B. Eden, T. O. McDonald, D. J. Adams, *Nat. Chem.* **2015**, *7*, 849–853; b) D. M. Raymond, B. L. Nilsson, *Chem. Soc. Rev.* **2018**, *47*, 3659–3720; c) H. Shigemitsu, T. Fujisaku, W. Tanaka, R. Kubota, S. Minami, K. Urayama, I. Hamachi, *Nat. Nanotechnol.* **2018**, *13*, 165–172; d) H. He, W. Tan, J. Guo, M. Yi, A. N. Shy, B. Xu, *Chem. Rev.* **2020**, *120*, 9994–10078; e) F. Sheehan, D. Sementa, A. Jain, M. Kumar, M. Tayarani-Najjaran, D. Kroiss, R. V. Ulijn, *Chem. Rev.* **2021**, *121*, 13869–13914; f) Z. Wang, Q. Wang, H. Cao, Z. Wang, D. Wang, J. Liu, T. Gao, C. Ren, J. Liu, *Adv. Mater.* **2024**, *36*, 2311043.
- [10] a) M. Gao, J. Deng, F. Liu, A. Fan, Y. Wang, H. Wu, D. Ding, D. Kong, Z. Wang, D. Peer, Y. Zhao, *Biomaterials* **2019**, *223*, 119486; b) X. Jiang, B. R. Stockwell, M. Conrad, *Nat. Rev. Mol. Cell Biol.* **2021**, *22*, 266–282.
- [11] a) X. Han, K. Cheng, Y. Xu, Y. Wang, H. Min, Y. Zhang, X. Zhao, R. Zhao, G. J. Anderson, L. Ren, G. Nie, Y. Li, *J. Am. Chem. Soc.* **2020**, *142*, 2490–2496; b) J. Zhan, Y. Cai, S. He, L. Wang, Z. Yang, *Angew. Chem. Int. Ed.* **2018**, *57*, 1813–1816.
- [12] B. Wu, S. Zhao, X. Yang, L. Zhou, Y. Ma, H. Zhang, W. Li, H. Wang, *ACS Nano* **2022**, *16*, 4126–4138.
- [13] a) H. N. Chang, B. Y. Liu, Y. K. Qi, Y. Zhou, Y. P. Chen, K. M. Pan, W. W. Li, X. M. Zhou, W. W. Ma, C. Y. Fu, Y. M. Qi, L. Liu, Y. F. Gao, *Angew. Chem. Int. Ed.* **2015**, *54*, 11760–11764; b) K. Cheng, Y. Ding, Y. Zhao, S. Ye, X. Zhao, Y. Zhang, T. Ji, H. Wu, B. Wang, G. J. Anderson, L. Ren, G. Nie, *Nano Lett.* **2018**, *18*, 3250–3258.
- [14] G. Wang, S. Chen, N. Qiu, B. Wu, D. Zhu, Z. Zhou, Y. Piao, J. Tang, Y. Shen, *Nano Today* **2021**, *39*, 101215.
- [15] a) V. Castelletto, I. W. Hamley, C. Cenko, U. Olsson, *J. Phys. Chem. B* **2010**, *114*, 8002–8008; b) K. Klement, K. Wieligmann, J. Meinhardt, P. Hortschansky, W. Richter, M. Fändrich, *J. Mol. Biol.* **2007**, *373*, 1321–1333.
- [16] S. Hohng, C. Joo, T. Ha, *Biophys. J.* **2004**, *87*, 1328–1337.
- [17] P. W. Gout, A. R. Buckley, C. R. Simms, N. Bruchovsky, *Leukemia* **2001**, *15*, 1633–1640.
- [18] a) M. Ramakrishnan, A. van Teijlingen, T. Tuttle, R. V. Ulijn, *Angew. Chem. Int. Ed.* **2023**, *62*, e202218067; b) E. R. Draper, B. Dietrich, K. McAulay, C. Brasnett, H. Abdizadeh, I. Patmanidis, S. J. Marrink, H. Su, H. Cui, R. Schweins, A. Seddon, D. J. Adams, *Matter* **2020**, *2*, 764–778; c) R. J. Swanekamp, J. T. M. DiMaio, C. J. Bowerman, B. L. Nilsson, *J. Am. Chem. Soc.* **2012**, *134*, 5556–5559; d) K. J. Nagy, M. C. Giano, A. Jin, D. J. Pochan, J. P. Schneider, *J. Am. Chem. Soc.* **2011**, *133*, 14975–14977.
- [19] S. Doll, B. Proneth, Y. Y. Tyurina, E. Panzilius, S. Kobayashi, I. Ingold, M. Irmler, J. Beckers, M. Aichler, A. Walch, H. Prokisch, D. Trümbach, G. W. Mao, F. Qu, H. Bayir, J. Füllekrug, C. H. Scheel, W. Wurst, J. A. Schick, V. E. Kagan, J. P. F. Angeli, M. Conrad, *Nat. Chem. Biol.* **2017**, *13*, 91–98.
- [20] L. H. Wang, K. G. Rothberg, R. G. Anderson, *J. Cell Biol.* **1993**, *123*, 1107–1117.
- [21] A. N. von Krusenstiern, R. N. Robson, N. Qian, B. Qiu, F. Hu, E. Reznik, N. Smith, F. Zandkarimi, V. M. Estes, M. Dupont, T. Hirschhorn, M. S. Shchepinov, W. Min, K. A. Woerpel, B. R. Stockwell, *Nat. Chem. Biol.* **2023**, *19*, 719–730.
- [22] K. Lei, A. Kurum, M. Kaynak, L. Bonati, Y. Han, V. Cencen, M. Gao, Y.-Q. Xie, Y. Guo, M. T. M. Hannebelle, Y. Wu, G. Zhou, M. Guo, G. E. Fantner, M. S. Sakar, L. Tang, *Nat. Biomed. Eng.* **2021**, *5*, 1411–1425.
- [23] a) S. J. Dixon, K. M. Lemberg, M. R. Lamprecht, R. Skouta, E. M. Zaitsev, C. E. Gleason, D. N. Patel, A. J. Bauer, A. M. Cantley, W. S. Yang, B. Morrison, 3rd, B. R. Stockwell, *Cell* **2012**, *149*, 1060–1072; b) E. Catanzaro, R. Demuyneck, F. Naessens, L. Galluzzi, D. V. Krysko, *Trends in Cancer* **2024**, *10*, 407–416.
- [24] a) X. Li, Y. Wang, Y. Zhang, C. Liang, Z. Zhang, Y. Chen, Z. W. Hu, Z. Yang, *Adv. Funct. Mater.* **2021**, *31*, 2100729; b) Y. Wang, X. Li, D. Zheng, Y. Chen, Z. Zhang, Z. Yang, *Adv. Funct. Mater.* **2021**, *31*, 2102505.
- [25] a) V. Cremasco, J. L. Astarita, A. L. Grauel, S. Keerthivasan, K. MacIsaac, M. C. Woodruff, M. Wu, L. Spel, S. Santoro, Z. Amoozgar, T. Laszewski, S. C. Migoni, K. Knoblich, A. L. Fletcher, M. LaFleur, K. W. Wucherpfennig, E. Pure, G. Dranoff, M. C. Carroll, S. J. Turley, *Cancer Immunol. Res.* **2018**, *6*, 1472–1485; b) L. Chen, T.-G. Huang, M. Meseck, J. Mandeli, J. Fallon, S. L. C. Woo, *Mol. Ther.* **2007**, *15*, 2194–2202.
- [26] a) J. Qian, S. Olbrecht, B. Boeckx, H. Vos, D. Laoui, E. Etliglu, E. Wauters, V. Pomella, S. Verbandt, P. Busschaert, A. Bassez, A. Franken, M. V. Bempt, J. Xiong, B. Weynand, Y. van Herck, A. Antoranz, F. M. Bosisio, B. Thienpont, G. Floris, I. Vergote, A. Smeets, S. Tejpar, D. Lambrechts, *Cell Res.* **2020**, *30*, 745–762; b) T. Ackermann, E. Shokry, R. Deshmukh, J. Anand, L. C. A. Galbraith, L. Mitchell, G. Rodriguez-Blanco, V. H. Villar, B. A. Sterken, C. Nixon, S. Zanivan, K. Blyth, D. Sumpton, S. Tardito, *EMBO Mol. Med.* **2024**, *16*, 2749–2774.
- [27] I. Sagiv-Barfi, H. E. Kohrt, D. K. Czerwinski, P. P. Ng, B. Y. Chang, R. Levy, *Proc. Natl. Acad. Sci. USA* **2015**, *112*, E966–E972.
- [28] P. Liao, W. Wang, W. Wang, I. Kryczek, X. Li, Y. Bian, A. Sell, S. Wei, S. Grove, J. K. Johnson, P. D. Kennedy, M. Gijon, Y. M. Shah, W. Zou, *Cancer Cell* **2022**, *40*, 365–378.

- [29] W. Zou, *Nat. Rev. Immunol.* **2006**, *6*, 295–307.
- [30] N. Nagarsheth, M. S. Wicha, W. Zou, *Nat. Rev. Immunol.* **2017**, *17*, 559–572.
- [31] a) J. Peng, B.-F. Sun, C.-Y. Chen, J.-Y. Zhou, Y.-S. Chen, H. Chen, L. Liu, D. Huang, J. Jiang, G.-S. Cui, Y. Yang, W. Wang, D. Guo, M. Dai, J. Guo, T. Zhang, Q. Liao, Y. Liu, Y.-L. Zhao, D.-L. Han, Y. Zhao, Y.-G. Yang, W. Wu, *Cell Res.* **2019**, *29*, 725–738; b) A. P. Patel, I. Tirosh, J. J. Trombetta, A. K. Shalek, S. M. Gillespie, H. Wakimoto, D. P. Cahill, B. V. Nahed, W. T. Curry, R. L. Martuza, D. N. Louis, O. Rozenblatt-Rosen, M. L. Suvà, A. Regev, B. E. Bernstein, *Science* **2014**, *344*, 1396–1401.

Manuscript received: November 7, 2024

Accepted manuscript online: December 25, 2024

Version of record online: January 8, 2025